

Carbon Nanotube with Vertical 2D Molybdenum Sulphoselenide Nanosheet Arrays for Boosting Electrocatalytic Hydrogen Evolution

Jing Yang,[†] Ying Liu,[†] Changshuai Shi,[‡] Jixin Zhu,[§] Xiaofei Yang,[#] Siliang Liu,[†] Le Li,[†] Ziwei Xu,^{*,‡} Chao Zhang,^{*,†} and Tianxi Liu^{*,†}

[†]State Key Laboratory for Modification of Chemical Fibers and Polymer Materials, College of Materials Science and Engineering, Innovation Center for Textile Science and Technology, Donghua University, Shanghai 201620, P. R. China

[‡]School of Materials Science & Engineering, Jiangsu University, Zhenjiang 212013, P. R. China

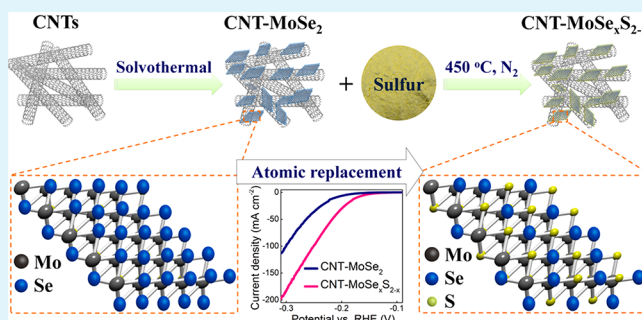
[§]Shaanxi Institute of Flexible Electronics (SIFE), Northwestern Polytechnical University (NPU), 127 West Youyi Road, Xi'an 710072, P. R. China

[#]College of Science, Nanjing Forestry University, Nanjing 210037, P. R. China

Supporting Information

ABSTRACT: Transition metal dichalcogenides (TMDs) are a promising non-noble-metal electrocatalyst toward the hydrogen evolution reaction (HER). However, the sluggish HER kinetics and poor electric conductivities of the TMDs severely restrict their practical applications for high-efficient water splitting. Herein, a nanosheet array of 2D anion-tailored $\text{MoSe}_x\text{S}_{2-x}$ on carbon nanotubes (CNTs) was prepared through an anionic substitution reaction. The all-solid-state sulfidation of the CNT- MoSe_2 precursor using the sulfur powder as the sulfur source indicates a green and easily scalable strategy for the preparation of the CNT- $\text{MoSe}_x\text{S}_{2-x}$ hybrid. As a result, the CNT- $\text{MoSe}_x\text{S}_{2-x}$ hybrid delivers an excellent HER performance including a low onset overpotential (83 mV), small Tafel slope (40 mV dec^{-1}) and long-term stability (overpotential at 10 mA cm^{-2} from 160 to 166 mV after 6000 cycles). The superior electrocatalytic activities of the CNT- $\text{MoSe}_x\text{S}_{2-x}$ hybrid are originated from decreased hydrogen adsorption energy associated with altering arrangements of Se and S atoms within the $\text{MoSe}_x\text{S}_{2-x}$ nanosheets. In addition, the $\text{MoSe}_x\text{S}_{2-x}$ nanosheet array on the highly conductive backbones of CNTs also enables an efficient electron/ion transport thus manifesting fast HER kinetics.

KEYWORDS: transition metal dichalcogenides, vertical nanosheet array, carbon nanotube, high-temperature sulfidation, hydrogen evolution



1. INTRODUCTION

Hydrogen, an ideal energy carrier with the highest energy density among various energy sources, has been intensively pursued to fulfill increasing energy demands in the coming energy crisis.^{1–3} In particular, the hydrogen evolution reaction (HER) in the electrochemical process has aroused extensive attentions as an efficient approach for sustainable hydrogen production.⁴ Platinum group catalysts (such as Pt and Pd) typically exhibit superior catalytic activities for the HER with a near zero onset potential, whereas their high cost and rare availability have severely restricted the large-scale productions of hydrogen.⁵ Therefore, the design and preparation of efficient and earth-abundant alternatives to Pt-based catalysts for water splitting remains key challenges to address the energy and environmental issues.^{6–9}

Two-dimensional (2D) transition metal dichalcogenides (TMDs) with a general formula of MX_2 , where M represents a transition metal and X represents a chalcogen (S, Se or Te), have attracted considerable attentions due to their high

electrochemical activities in energy conversions.^{10–14} Among numerous candidates of the TMDs such as MoS_2 ,¹⁵ CoS_2 ,¹⁶ CoSe_2 ,¹⁷ and WS_2 ,¹⁸ MoSe_2 is gradually emerging as an efficient HER catalyst due to its narrower band gap of ~ 1.4 eV.^{2,19} Unfortunately, the poor electric conductivity as well as the easy agglomeration of 2D MoSe_2 nanosheets has significantly restricted its catalytic performance toward the HER.^{2,20} Theoretical calculations have revealed that the HER activity of the 2D TMDs is strongly associated with the number of electrochemically active sites,^{21,22} which was also validated by several evidence from the experimental views.^{23,24} Accordingly, many efforts have been made to further improve the electrocatalytic performance of the MoSe_2 through preserving their easy aggregation by coupling them with conductive materials, such as carbon cloth,²⁵ graphene and

Received: August 31, 2018

Accepted: November 21, 2018

Published: November 21, 2018

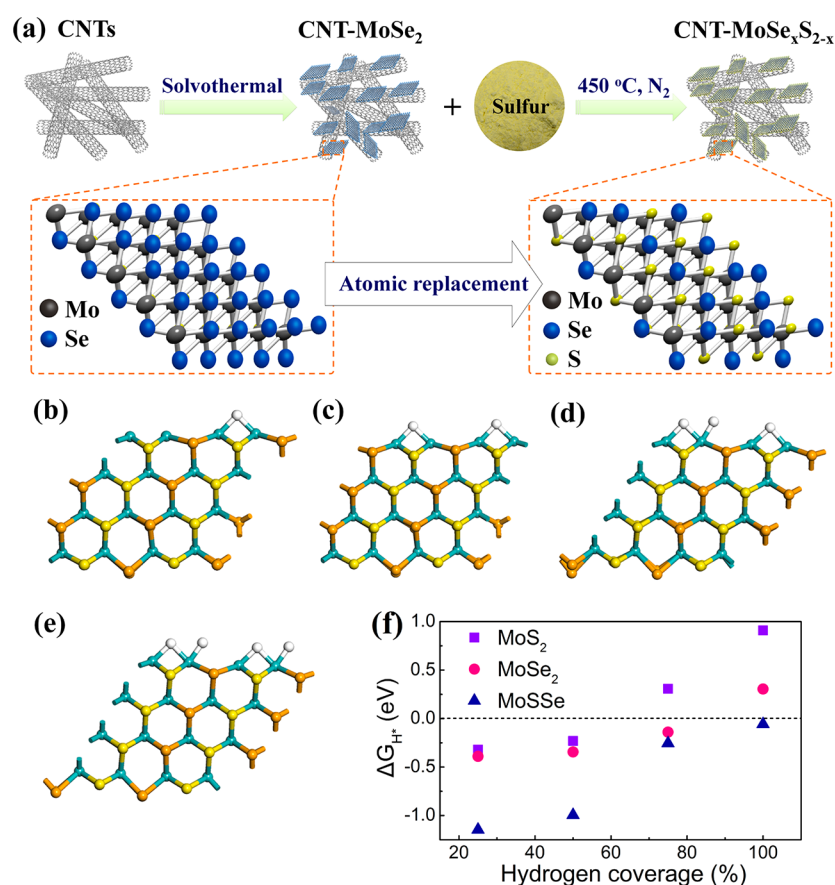


Figure 1. (a) Schematic illustration of the synthesis of the CNT-MoSe_xS_{2-x} hybrid. Optimized structure of (b) MoS₂-H, (c) MoSe₂-2H, (d) MoSSe-3H, and (e) MoSSe-4H, where the white, cyan, yellow, and orange balls represent the H, Mo, S, and Se atoms, respectively. (f) ΔG_{H*} of the hydrogen adsorptions on Mo edges of the MoS₂, MoSe₂, and MoSSe at the hydrogen coverage 25, 50, 75, and 100%, respectively.

carbon nanotubes,^{26,27} thus exposing more active sites as well as improving the electric conductivity of the catalysts. Solvothermal reactions²⁸ and chemical vapor depositions (CVD)²⁹ are commonly methods applied to effectively prepare the 2D MoSe₂ nanostructure. Nevertheless, the aforementioned methods requiring complex preparation approaches (high cost and large energy consumption) unquestionably restrict their future applications. Therefore, it is still a great challenge to develop a simple and efficient method to prepare the TMD-based hydrogen evolution catalysts with improved electron transfer, increased number of exposed active sites and enhanced catalytic activity of active sites to synergistically boost the resultant HER activity.^{30–32}

Herein, we present a design and targeted synthesis of carbon nanotube (CNT)-backboned MoSe_xS_{2-x} through an “all-in-crucible” solid-state sulfidation reaction. Among the hybrid catalysts, the MoSe_xS_{2-x} nanosheet array provides abundant active sites, and the CNT backbone enables fast electron transport thus yielding superior electrochemical activities and stabilities for the HER. More importantly, the MoSe_xS_{2-x} with a tunable Se/S ratio dramatically reduces the hydrogen adsorption energy on the Mo-edge adsorption thus resulting in significantly boosted activity for the HER. The atomic replacements of Se with S would not damage the Se–Mo–Se sandwich structure within the nanosheets, thereby maintaining the structural and durable stability. Compared with conventional solution-processed sulfidation with an extremely low yield and high energy consumption/cost, the solid-state sulfidation provides an easily scalable route for the synthesis

of anion-tunable MoSe_xS_{2-x} nanostructures. This study therefore opens a new guideline of developing highly efficient HER catalysts based on 2D TMD-based materials.

2. EXPERIMENTAL SECTION

2.1. Materials. CNTs (outer diameter of 20–30 nm) were supplied by Chengdu Institute of Organic Chemistry, Chinese Academy of Sciences, China. Sodium molybdate dehydrate (Na₂MoO₄·2H₂O, AR), Se powder (CP), sublimed sulfur (CP), and hydrazine hydrate (N₂H₄·H₂O, 85%) were provided by Sinopharm Chemicals. Pt/C catalyst was purchased from Alfa Aesar. Ammonium tetrathiomolybdate ((NH₄)₂MoS₄, AR) was purchased from Sigma-Aldrich. N,N-Dimethylformamide (DMF) and ethanol were obtained from Shanghai Chemicals. All aqueous solutions were prepared with deionized (DI) water.

2.2. Preparation of the CNT-MoSe₂ and CNT-MoS₂. The CNT-MoSe₂ hybrid was prepared through solvothermal method for the growth of MoSe₂ using acid-treated CNTs as the template. The acid-treated CNTs were obtained by refluxing raw CNTs in an acid mixture (H₂SO₄/HNO₃ = 3/1 in v/v) at 70 °C for 1 h. Upon filtration, washing and drying, 50 mg of acid-treated CNTs was suspended in 25 mL of DMF by sonication. Meanwhile, 50 mg of Se powder was dispersed in 25 mL of 85% hydrazine hydrate at 80 °C to form a red-brown solution. Subsequently, 25 mL of Se/hydrazine hydrate solution was added into the DMF suspension of acid-treated CNTs with a stoichiometric amount of Na₂MoO₄ at a Mo/Se molar ratio of 1/2. The mixture was transferred to a 100 mL Teflon-lined autoclave and heated at 180 °C for 12 h with a heating rate of 5 °C min⁻¹. The products were collected by filtration, washed with DMF and DI water for several times, and dried at 60 °C in vacuum. The initial concentrations of the Se solutions were controlled to be 1, 2,

Table 1. Comparison of Chemical Compositions and Electrochemical Performances of the CNT-MoSe₂, CNT-MoSe_xS_{2-x} and CNT-MoS₂

samples	Se:S ratio		onset (mV)	$\eta@10 \text{ mA cm}^{-2}$ (mV)	Tafel slope (mV dec ⁻¹)
	ICP	XPS			
CNT-MoSe ₂			-117	213	46
CNT-MoSe _{0.93} S _{1.07}	0.93:1.07	0.89:1.11	-87	180	43
CNT-MoSe _{1.06} S _{0.94}	1.06:0.94	1.06:0.94	-83	174	40
CNT-MoSe _{1.20} S _{0.80}	1.20:0.80	1.12:0.88	-126	204	44
CNT-MoS ₂			-93	224	52

and 3 mg mL⁻¹, respectively, to optimize the MoSe₂ loadings on the CNTs, denoted as CNT-MoSe₂-1, CNT-MoSe₂-2 and CNT-MoSe₂-3, respectively. Similarly, the CNT-MoS₂ hybrid was prepared by solvothermal method using DMF as the solvent. Eight milligrams of acid-treated CNTs, 80 mg of (NH₄)₂MoS₄ and 0.8 mL of 85% hydrazine hydrate was suspended into 40 mL of DMF. The mixture was transferred into a 50 mL Teflon-lined stainless steel autoclave, heated at 200 °C for 10 h with a heating rate of 5 °C min⁻¹. The products were collected by filtration, washed with DMF and ethanol several times, and dried at 60 °C in vacuum. For comparison, neat MoSe₂ and MoS₂ were prepared by the similar method without CNTs.

2.3. Preparation of the CNT-MoSe_xS_{2-x}. The CNT-MoSe_xS_{2-x} hybrid with a tunable Se/S ratio was prepared by high-temperature sulfidation using the CNT-MoSe₂ and sulfur powder as the precursor and sulfur sources, respectively, in a tube furnace with a quartz tube. A covered ceramic boat containing the mixture of the CNT-MoSe₂ and sulfur powder was heated to a certain temperature at a ramp of 5 °C min⁻¹ and held for 2 h under a nitrogen flow. The Se/S ratios were tailored by varying the mass ratios of the CNT-MoSe₂ and sulfur (1/2, 1/4, and 1/6), thus giving the CNT-MoSe_{1.20}S_{0.80}, CNT-MoSe_{1.06}S_{0.94} and MoSe_{0.93}S_{1.07} (calculated from the inductively coupled plasma-optical emission spectroscopy (ICP-OES)). The sulfidation temperature was tailored at 350, 450, and 550 °C, respectively, with a 1/4 mass ratio of CNT-MoSe₂ and sulfur. For comparison, a reference sample was also prepared through the above-mentioned process in the absence of CNTs. The mass ratios of the MoSe₂ and sulfur were kept at 1/4 to get neat MoSe_{1.05}S_{0.95} during the sulfidation process.

3. RESULTS AND DISCUSSION

The preparation of the CNT-MoSe_xS_{2-x} hybrid mainly consists of two steps demonstrated in Figure 1a. First, the CNT-MoSe₂ was prepared via solvothermal growth of 2D MoSe₂ on acid-treated CNTs. The oxygen functional groups on acid-treated CNTs benefit the array decoration of 2D MoSe₂. The density of MoSe₂ nanosheet array on CNTs could be easily tuned with different initial Se concentrations of 1, 2, and 3 mg mL⁻¹, respectively, and the products were denoted as CNT-MoSe₂-1, CNT-MoSe₂-2, and CNT-MoSe₂-3, respectively. Unless otherwise specified, the CNT-MoSe₂ appearing on its own refers to the CNT-MoSe₂-2 in the following. Second, the CNT-MoSe_xS_{2-x} hybrid was prepared via thermal sulfidation of CNT-MoSe₂ using the powder sulfur sources. By tuning the mass ratios of CNT-MoSe₂ to sulfur as well as the sulfidation temperatures, the Se/S ratio among the MoSe_xS_{2-x} could be precisely tailored. In details, the mass ratios of CNT-MoSe₂ to sulfur powder were tuned to be 1/2, 1/4 and 1/6, respectively, at the sulfidation temperature of 450 °C, and the products were calculated to be CNT-MoSe_{1.20}S_{0.80}, CNT-MoSe_{1.06}S_{0.94} and CNT-MoSe_{0.93}S_{1.07}, respectively, based on the elemental analysis using inductively coupled plasma-optical emission spectroscopy (ICP-OES). Besides, the Se/S molar ratios among the CNT-MoSe_xS_{2-x} hybrid were also calculated from the X-ray photoelectron spectroscopy (XPS) (Table 1). The

XPS results generally provide the surface elemental compositions of measured samples due to X-ray cannot penetrate into interiors of measured samples.^{33,34} However, the elemental composition results acquired from the ICP-OES correspond to the total elemental contents within measured samples.^{35,36} Hence, the Se/S ratios derived from XPS and ICP-OES are of a little difference.

The target products CNT-MoSe_xS_{2-x} with rationally designed compositional and structural features could greatly boost their catalytic properties by synergistically increasing the number of active sites and enhancing the catalytic activity of active sites for the HER. In order to make clear that why the MoSe_xS_{2-x} structures show superior catalytic performance than neat MoS₂ and MoSe₂, the MoSSe with a Se/S ratio of 1:1 (see the top and side views of the build slab of pristine MoSSe adopted in the DFT calculations in Figure S1) was calculated and expected to decrease the Gibbs free energy for hydrogen adsorption (ΔG_{H^*}). In principle, the data of ΔG_{H^*} is theoretically used to evaluate the HER activity of active sites of a catalyst.^{17,37} Low ΔG_{H^*} will cause a strong and sufficient adsorption of H atoms, while high ΔG_{H^*} will make the H atoms bonded too weakly on the catalyst surface.³⁸ The Sabatier “volcano” plot indicates that ΔG_{H^*} of an ideal HER catalyst is required to be close to thermoneutral ($\Delta G_{H^*} = 0$), where a good balance between the adsorption and desorption of hydrogen can be achieved.⁴ Therefore, herein density functional theory (DFT) calculations were carried out to evaluate the impact on the intrinsic catalytic activity of MoSe₂ with an anion replacement (see the Supporting Information for detailed computation details and theoretical models). Basically, the pathway for the electrocatalytic HER can be defined into three stages, i.e., an initial state (H⁺), an intermediate state (H^{*}) and a final state (1/2 H₂). The ΔG_{H^*} is a key parameter for evaluating the final HER activity of a catalyst, and the catalyst with a ΔG_{H^*} closer to thermoneutral could be considered as an ideal candidate as a HER catalyst. According to previous studies, the HER sites of the MoS₂ as well as its analogues like MoSe₂ are mainly ascribed to exposed edges.³⁹⁻⁴² particularly the metallic edges like Mo atoms. Therefore, we still considered the Mo-edge adsorption similar to the model used in the previous calculation of MoSe₂.⁴³ Figure 1b–e indicates optimized structures of (b) MoSSe-H, (c) MoSSe-2H, (d) MoSSe-3H, and (e) MoSSe-4H. The white, cyan, yellow, and orange balls represent the H, Mo, S, and Se atoms, respectively. The hydrogen atoms with the number of 1, 2, 3, and 4 are adsorbed on the edge Mo atoms with the coverage of 25, 50, 75, and 100%, respectively. Interestingly, the optimized configurations show that the adsorbed hydrogen prefers diffusing into the middle of two neighboring Mo atoms rather than attaching to the Mo atoms by “face-to-face” ways, which are quite different with the adsorbed hydrogen on the Mo edge of MoSe₂.⁴⁴ The adsorbed

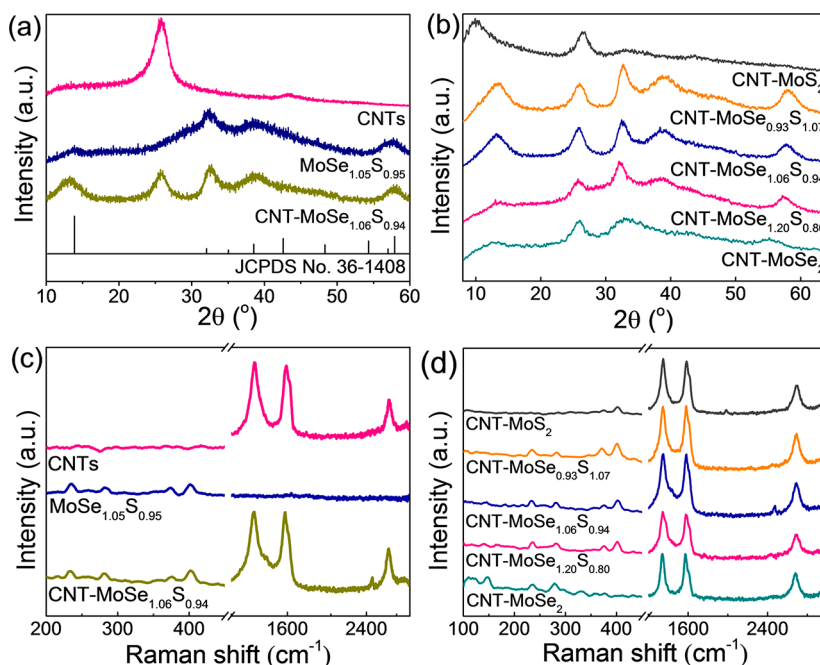


Figure 2. (a) XRD patterns of the CNTs, $\text{MoSe}_{1.05}\text{S}_{0.95}$, and $\text{CNT-MoSe}_{1.06}\text{S}_{0.94}$; (b) XRD patterns of the CNT-MoS_2 , $\text{CNT-MoSe}_{0.93}\text{S}_{1.07}$, $\text{CNT-MoSe}_{1.06}\text{S}_{0.94}$, $\text{CNT-MoSe}_{1.20}\text{S}_{0.80}$, and CNT-MoS_2 ; (c) Raman spectra of the CNTs, $\text{MoSe}_{1.05}\text{S}_{0.95}$, and $\text{CNT-MoSe}_{1.06}\text{S}_{0.94}$; (d) Raman spectra of the CNT-MoS_2 , $\text{CNT-MoSe}_{0.93}\text{S}_{1.07}$, $\text{CNT-MoSe}_{1.06}\text{S}_{0.94}$, $\text{CNT-MoSe}_{1.20}\text{S}_{0.80}$, and CNT-MoS_2 .

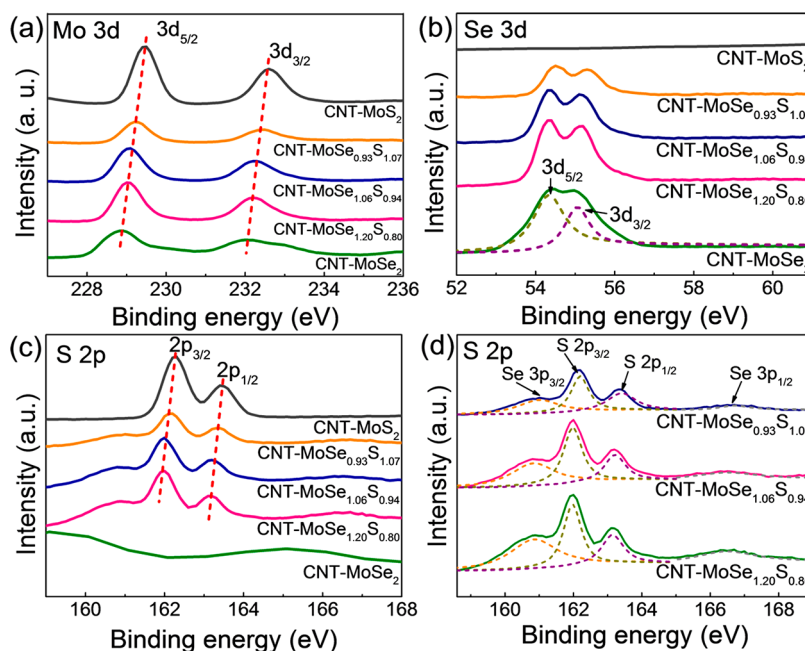


Figure 3. (a) Mo 3d, (b) Se 3d, and (c) S 2p XPS spectra of the CNT-MoS_2 , $\text{CNT-MoSe}_{0.93}\text{S}_{1.07}$, $\text{CNT-MoSe}_{1.06}\text{S}_{0.94}$, $\text{CNT-MoSe}_{1.20}\text{S}_{0.80}$ and CNT-MoS_2 . (d) S 2p XPS spectra of the $\text{CNT-MoSe}_{0.93}\text{S}_{1.07}$, $\text{CNT-MoSe}_{1.06}\text{S}_{0.94}$ and $\text{CNT-MoSe}_{1.20}\text{S}_{0.80}$.

hydrogen atoms are actually shared by the edge Mo atoms indicating their relatively weaker interactions, which may be attributed to lattice deformations of the edges created by the replacement of the S with Se. More impressively, the ΔG_{H^*} in Figure 1f shows that there are big improvements of the HER activity of the MoSSe with the calculated ΔG_{H^*} of approximately -0.056 eV at the hydrogen coverage of 100% with details showed in Table S1. Such a value is very close to the thermoneutral criterion and is even closer than the one of Pt ($\Delta G_{\text{H}^*} \approx -0.09$ eV) reported previously.⁴⁵ Considering the

inevitable calculation errors (say, $|\Delta| \approx 0.05$ eV) introduced by using different models, different parameters and different reference data adopted in the calculation, we can estimate the $\Delta G_{\text{H}^*} - |\Delta| \approx -0.11$ eV, which is still closer to the thermoneutral than the best $\Delta G_{\text{H}^*} = -0.23$ eV and $\Delta G_{\text{H}^*} = -0.14$ eV for the MoS_2 and MoSe_2 reported by previous studies.^{43,46} Furthermore, different with the MoS_2 and MoSe_2 , the ΔG_{H^*} of MoSSe in Figure 1f rise monotonously with the increase of the hydrogen coverage and reach the best HER performance at a 100% hydrogen coverage. This means more

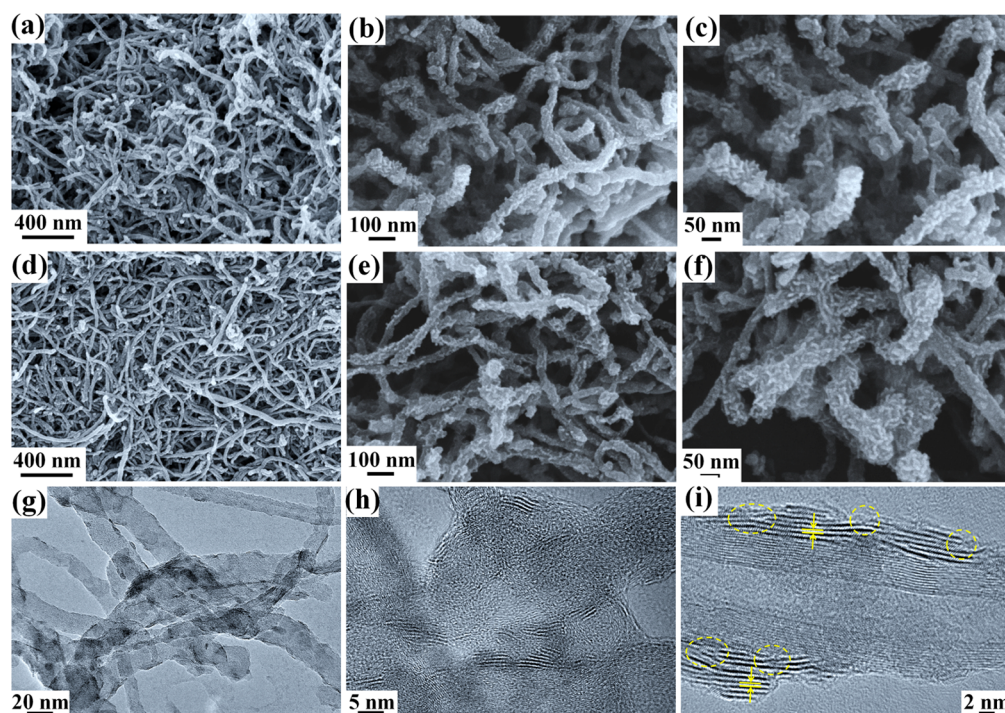


Figure 4. SEM images of (a–c) CNT-MoSe₂ and (d–f) CNT-MoSe_{1.06}S_{0.94}. (g–i) TEM images of CNT-MoSe_{1.06}S_{0.94} with folded edges of the MoSe_{1.06}S_{0.94} nanosheets. The dotted circular frames in i indicate the crystal distortions and defective sites of MoSe_{1.06}S_{0.94} nanosheets.

hydrogen can be catalyzed at the edge of the MoSSe. Such a big improvement of the HER activity may be attributed to the deformed lattice of the edge of MoSSe as well as the shared bonding between one hydrogen and two neighboring Mo atoms, leading to weaker interactions between adsorbed hydrogen and the edge of the MoSSe compared with the MoS₂ and MoSe₂.

Figure 2a indicates the X-ray diffraction (XRD) patterns of the CNT-MoSe_xS_{2-x} hybrid revealing the compositions and crystal structures of the catalysts. The diffraction patterns at $2\theta = 26.0^\circ$ of the CNTs and CNT-MoSe_{1.06}S_{0.94} can be assigned to (002) plane of the sidewalls of CNTs. For the MoSe_{1.05}S_{0.95}, the XRD pattern displays the expected characteristic hexagonal molybdenum dichalcogenide features and the reflections in $2\theta = 14.0, 32.1, 38.6,$ and 58.0° match the (002), (100), (103), and (008) crystal planes of MoS_{1.0}Se_{1.0} (JCPDS No. 36–1408). Moreover, all the patterns are broadened indicating a decrease in their structural crystallinity.⁴⁷ For comparison, Figure 2b indicates that the diffraction patterns at $2\theta = 13.4, 32.7,$ and 56.3° in the CNT-MoSe₂ correspond to (002), (100) and (110) planes of hexagonal 2H-phase MoSe₂ (JCPDS No. 87–2419). The diffraction patterns ascribed to (110) plane of MoSe₂ increase to higher angles as the S contents increase within the MoSe_xS_{2-x} (Figure 2b). Such an upshift is attributed to the replacement of large-diameter Se with small-diameter S atoms, which is in accordance with the decrease in lattice parameters caused by the incorporation of S atoms within transition-metal selenides.^{2,19}

Raman spectroscopy was conducted to investigate phonon vibration mode properties of the CNT-MoSe_xS_{2-x}. The Raman spectra of CNTs reveal the characteristic peaks of D, G and 2D bands at 1353, 1592, and 2702 cm⁻¹, respectively (Figure 2c). The Raman spectra at low frequencies (200–500 cm⁻¹) of MoSe_{1.05}S_{0.95} and CNT-MoSe_{1.06}S_{0.94} include the Mo–Se and Mo–S related modes, respectively. With the incorporation of S

atoms within the MoSe_xS_{2-x}, the original MoSe₂ crystal symmetry is destroyed due to lattice distortion from the substitution of Se with smaller S atoms.^{2,48} Therefore, the two vibration modes shift to a higher frequency due to the local stress caused by the incorporation of S atoms into MoSe₂ (Figure 2d).⁴⁹ In addition, the characteristic peaks of 2H-phase MoSe₂ locate at 235.1 and 283.4 cm⁻¹, which correspond to in-plane E_{2g}¹ and out-of-plane A_{1g}, respectively. With the increase of S contents, the intensities of MoS₂-like bands increased along with the significant peaks of in-plane E_{2g}¹ (375.5 cm⁻¹) and out-of plane A_{1g} (400.9 cm⁻¹) vibration modes, while the intensities of MoSe₂-like bands intensely decrease.

XPS measurements were utilized to further investigate the binding energies and chemical compositions of the CNT-MoSe_xS_{2-x} and the corresponding high-resolution spectra of Mo 3d, Se 3d and S 2p were displayed in Figure 3. The Mo 3d_{5/2} and Mo 3d_{3/2} characteristic peaks centered at 228.9 and 232.1 eV manifest the Mo⁴⁺ oxidation state in the hexagonal 2H phase of MoSe₂ (Figure 3a). The incorporations of S atoms within the MoSe_xS_{2-x} nanosheets lead to a continuous displacement of Mo 3d_{5/2} peak to higher binding energy (MoSe₂: 228.9 eV, MoS₂: 229.4 eV), which are caused by the increase of nominal valence state of Mo for the higher electronegativity of S than that of Se.⁵⁰ By controllably regulating the Se/S molar ratios, the 3d band electronic structure of Mo can be elaborately modified. As the 3d band electrons in transition metals are involved in bonding with the adsorbates, subtle modification in the d band electronic structure may give rise to the effective optimization in the catalytic activity of MoSe_xS_{2-x}.^{2,51,52} Moreover, the corresponding changes can be also observed in the Se 3d (Figure 3b) and S 2p (Figure 3c) XPS spectra with an increase of S contents. The decrease in the proportion of S atoms within the MoSe_xS_{2-x} leads to a continuous displacement of S 2p_{3/2} and S 2p_{1/2} peaks to higher binding energy, indicating the

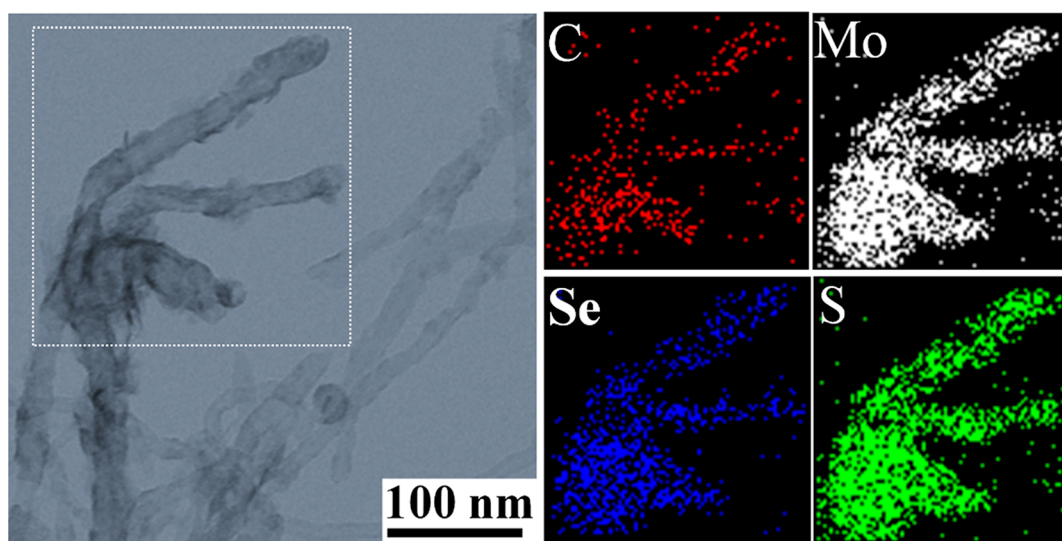


Figure 5. TEM-EDX elemental mappings of the CNT-MoSe_{1.06}S_{0.94} showing the homogeneous distributions of the C (red), Mo (white), Se (blue), and S (green) elements.

sulfurization processes take effect at selected experimental conditions. The XPS peaks of the CNT-MoSe_xS_{2-x} between 158 and 169 eV can be deconvoluted into four peaks (Figure 3d). The peaks located at 163.2 and 162 eV correspond to the S 2p_{1/2} and S 2p_{3/2} orbitals of MoSe_xS_{2-x}, indicating the existence of Mo–S bonding instead of elemental S, whereas the other two peaks at 160.8 and 166.5 eV are attributed to the binding energies of Se 3p_{3/2} and 3p_{1/2}, respectively.

The morphological evolutions from the CNT-MoSe₂ to CNT-MoSe_{1.06}S_{0.94} are monitored by scanning electron microscopy (SEM) and transmission electron microscopy (TEM) in Figure 4. The acid-treated CNTs with a smooth surface are interpenetrating with each other (Figure S2a, b). After solvothermal growth of MoSe₂, the significantly rough surface of CNTs indicates the vertical decoration of MoSe₂ nanosheet array (Figure 4a–c). However, without the CNT templates, neat MoSe₂ displays a 2D MoSe₂-assembled flower-like structure (Figure S2c, d). In addition, the density of MoSe₂ nanosheet array could be easily tailored by tuning different MoSe₂ loadings. When the Se concentration is relatively low (1 mg mL⁻¹), only few unapparent small particles are scattered on the surface of CNTs, and the diameter of CNT-MoSe₂-1 shows a slight increase compared with neat CNTs (Figure S3a, b). With the increase in Se contents to be 3 mg mL⁻¹ for the CNT-MoSe₂-3, perpendicularly oriented MoSe₂ nanosheets with a denser distribution are observed on the surface of CNTs, and excess MoSe₂ aggregates into flowerlike MoSe₂ microspheres (Figure S3c, d). TEM characterizations are carried out to distinguish the morphologies between the CNT-MoSe₂-1 and CNT-MoSe₂-2 (Figure S4). For the CNT-MoSe₂-1, only few MoSe₂ nanosheets are scattered on the CNTs along the axial direction. However, vertically aligned MoSe₂ nanosheet arrays among the CNT-MoSe₂-2 are observed. Upon sulfidation, the MoSe_{1.06}S_{0.94} nanosheet array within the CNT-MoSe_{1.06}S_{0.94} maintains well, indicating the atomic substitution of Se with S atoms does not destroy the lamellar structures of MoSe₂ (Figure 4d–f). Thin layers of MoSe_{1.06}S_{0.94} nanosheets are uniformly decorated on the CNTs with stretching-out folded edges (Figure 4g–i). The interlayer distance of the MoSe_{1.06}S_{0.94} nanosheets is ~0.65 nm corresponding to the

(002) plane orientation of 2H-phase MoSe₂. The thickness of the MoSe_{1.06}S_{0.94} nanosheets can be estimated by the curve edges of the nanosheets in cross-section TEM images, which are determined in the range of 1.3–6.5 nm with a thickness of 2–10 atomic layers. The MoSe_{1.06}S_{0.94} nanosheets are tightly grown on the CNTs and the resultant frameworks are interconnected with each other to create a highly porous structure, which therefore facilitates ion/electron diffusion pathways. The lattice fringes along the curled MoSe_{1.06}S_{0.94} edges are discontinuous, indicating the formation of numerous crystal distortions and dislocations (marked in dotted circular frames in Figure 4i). Such crystal defects can afford the additional defective edge sites, thus enhancing the resultant catalytic properties. Moreover, the energy dispersive X-ray (EDX) mappings further manifest a uniform distribution of C, Mo, Se, S elements in the CNT-MoSe_{1.06}S_{0.94} sample (Figure 5).

The linear sweep voltammetry (LSV) measurements are conducted to evaluate the HER performance of the CNT-MoSe₂ with different loadings of MoSe₂ by using a typical three-electrode electrochemical cell in a N₂-saturated 0.5 M H₂SO₄ electrolyte. The CNT-MoSe₂-2 electrode displays a catalytic activity with an overpotential of 213 mV at 10 mA cm⁻² (Figure S5a), which is lower than those of CNT-MoSe₂-1 (244 mV) and CNT-MoSe₂-3 (237 mV). Furthermore, electrochemical impedance spectroscopy (EIS) was applied to characterize the HER reaction processes catalyzed by CNT-MoSe₂-1, CNT-MoSe₂-2 and CNT-MoSe₂-3 electrodes in Figure S6. All Nyquist plots of each electrode have two semicircles. The difference of the three plots is significant. The semicircle at lower frequencies is potential-dependent and represents the charge transfer process. The semicircle at higher frequencies represents a time constant that is largely potential-independent and is most probably related to the contact resistance between the glassy carbon electrode and the catalyst. Among all CNT-MoSe₂ samples, the CNT-MoSe₂-2 electrode shows a minimum charge transfer resistance (R_{ct}) and contacting resistance together compared with those of the CNT-MoSe₂-1 and CNT-MoSe₂-3 electrodes, indicating a faster charge transfer during the electrochemical process. Therefore, the catalytic activity differences can be explained

according to the different morphology and R_{ct} of the resultant catalysts. For CNT-MoSe₂-1, only sparsely MoSe₂ nanosheets are anchored on CNT backbones and some regions of CNT backbones are exposed without the coverage of MoSe₂ active sites. For CNT-MoSe₂-3, excess MoSe₂ aggregates decrease the exposure of MoSe₂ active sites, restricting the ion/electron transfer and electrolyte diffusion. Therefore, the CNT-MoSe₂-2 with a moderate MoSe₂ loading offers optimized conductivities and more exposed active sites, thus exhibiting optimal catalytic performance. Therefore, the CNT-MoSe₂-2 precursor is chosen for subsequent sulfidation. Sulfidation temperatures of 350, 450, and 550 °C are conducted to evaluate the sulfidation temperature on the HER activity of the resultant catalysts. The CNT-MoSe_xS_{2-x} catalysts prepared at 350, 450, and 550 °C, respectively, exhibit overpotentials of 188, 174, and 208 mV, respectively, at 10 mA cm⁻² (Figure S5b). When the sulfidation temperature is 350 °C, only a small amount of sulfur can be successfully doped into MoSe₂ in 2 h due to relatively slow reaction process. However, when the sulfidation temperature is 550 °C, most of sulfur may suffer fast evaporation during the sulfidation, similarly leading to fewer sulfur doping. Therefore, a moderate amount of sulfur can be controllably doped into MoSe₂ nanosheets by controlling the appropriate temperature at 450 °C. Meanwhile, based on the XPS results and relative analysis in Supporting Information, the CNT-MoSe_xS_{2-x} can be tuned to be CNT-MoSe_{1.20}S_{0.80}, CNT-MoSe_{1.06}S_{0.94} and CNT-MoSe_{0.93}S_{1.07}, with an initial mass ratio of the CNT-MoSe₂ precursor to sulfur powder of 1/2, 1/4, and 1/6, respectively. The CNT-MoSe_{1.20}S_{0.80}, CNT-MoSe_{1.06}S_{0.94} and CNT-MoSe_{0.93}S_{1.07} catalysts show overpotentials of 204, 174, and 180 mV, respectively, at 10 mA cm⁻² (Figure S5c, d and Table 2). The CNT-MoSe_{1.06}S_{0.94} electrode exhibits lower

Table 2. Comparison of Electrochemical Properties of CNT-MoSe_xS_{2-x}-Related Samples

samples	onset (mV)	$\eta@10 \text{ mA cm}^{-2}$ (mV)	Tafel slope (mV dec ⁻¹)
CNTs			
MoSe ₂	-148	366	69
MoSe _{1.05} S _{0.95}	-120	303	60
MoS ₂	-193	347	103
CNT-MoSe ₂	-117	212	46
CNT-MoSe _{1.06} S _{0.94}	-83	174	40
CNT-MoS ₂	-93	224	52
Pt/C	-9	30	31

onset overpotential of 83 mV than those of CNT-MoSe₂ (117 mV) and CNT-MoS₂ (93 mV) (Figure 6a and Table 2). Meanwhile, the overpotentials of CNT-MoSe_{1.06}S_{0.94}, CNT-MoSe₂ and CNT-MoS₂ are measured to be 174, 213, and 224 mV at 10 mA cm⁻², respectively. The commercial Pt/C catalyst was also tested for comparison, exhibiting the catalytic performance for HER with a near zero onset potential and an overpotential of 30 mV at 10 mA cm⁻². The positive effects of introducing highly conductive CNTs as a backbone were investigated. As shown in Figure 6b, the polarization curve of CNTs indicates that there is negligible electrochemical HER activity for neat CNTs. However, the CNT-MoSe_{1.06}S_{0.94} electrode exhibits an overpotential of 117 mV at a current density of 10 mA cm⁻², which is much smaller than that of neat MoSe_{1.05}S_{0.95} catalyst with a similar Se/S ratio (the overpotential at 10 mA cm⁻²: 303 mV). Furthermore, Brunauer–

Emmett–Teller (BET) theory and pore size distributions based on nonlocal density functional theory (NLDFT) slit pore model were calculated for the CNT, CNT-MoSe_{1.06}S_{0.94} and MoSe_{1.05}S_{0.95}. The specific surface area of CNT-MoSe_{1.06}S_{0.94} composite is calculated to be 61.4 m² g⁻¹, which is apparently larger than that of MoSe_{1.05}S_{0.95} nanosheets (9.9 m² g⁻¹) in Figure S7. A higher surface area can provide more active sites, thus giving rise to better catalytic activity for HER. Therefore, 1D CNT templates may afford a uniform dispersion of MoSe_xS_{2-x} nanosheets without aggregations, offering an abundance of accessible active sites for sequent electrocatalysis. Besides, the interconnected CNT network may facilitate the electron transport from active sites to current collectors.

Tafel analysis by fitting the linear portion of Tafel plot was utilized to study the HER kinetics, according to the Tafel equation: $\eta = b \log j + a$, where η , b and j represent overpotential, Tafel slope and current density, respectively. The Tafel slope is closely related to the reaction pathway and adsorption types, which can reflect an inherent property of catalyst. Three major reaction mechanisms have been involved in the HER in acidic electrolytes:⁵³ (1) Discharge step (Volmer reaction): $\text{H}_3\text{O}^+ + \text{e}^- \rightarrow \text{H}_{\text{ads}} + \text{H}_2\text{O}$, where a proton is absorbed on an active edge site, achieving a Tafel slope of $\sim 120 \text{ mV dec}^{-1}$; (2) Electrochemical desorption step (Heyrovsky reaction): $\text{H}_{\text{ads}} + \text{H}_3\text{O}^+ + \text{e}^- \rightarrow \text{H}_2 + \text{H}_2\text{O}$, where an H_{ads} combines with a proton in the aqueous solution to convert H^+ to H_2 with a Tafel slope of $\sim 40 \text{ mV dec}^{-1}$; (3) Tafel recombination step (Tafel reaction): $\text{H}_{\text{ads}} + \text{H}_{\text{ads}} \rightarrow \text{H}_2$, where the chemisorption of hydrogen (H_{ads}) migrates over the electrode surface to interact with immobile adsorbed atoms to form molecular hydrogen (spillover effect),¹⁵ leading to a Tafel slope of $\sim 30 \text{ mV dec}^{-1}$. Therefore, the Volmer–Heyrovsky or Volmer–Tafel mechanism should be involved in the electrochemical HER process to produce molecular hydrogen.¹⁵ As shown in Figure 6c, the Tafel slopes obtained from the CNT-MoS₂, CNT-MoSe₂, and CNT-MoSe_{1.06}S_{0.94} electrodes are 52, 46, and 40 mV dec⁻¹, respectively. The Tafel slopes between 40 and 70 mV dec⁻¹ are ascribed to the Volmer–Heyrovsky mechanism with a fast discharge reaction followed by an electrochemical desorption step as the rate-limiting step. With a small Tafel slope of 40 mV dec⁻¹, the CNT-MoSe_{1.06}S_{0.94} catalyst suggests a Tafel-step-determined Volmer–Tafel mechanism, where the chemisorption of hydrogen from electrolytes onto the surface requires little activation energy.⁴⁸ Therefore, the small Tafel slope of the CNT-MoSe_{1.06}S_{0.94} electrode with an enhanced HER rate of a moderate overpotential increase is definitely beneficial in practical applications.⁵⁴ A comparison of catalytic properties between the CNT-MoSe_{1.06}S_{0.94} and MoSe_xS_{2-x}-based electrocatalysts in the literatures is presented in Table 3. The lower overpotential and Tafel slope of CNT-MoSe_{1.06}S_{0.94} are comparable to most previously reported catalysts, indicating that the element doping or hybridization with conductive materials plays important roles in designing highly active MoS₂- or MoSe₂-based electrocatalysts. Moreover, the exchange current densities (j_0) can be determined by applying extrapolation method to the Tafel plots. Figure S8 indicates the calculation of j_0 for the MoSe₂, MoSe_xS_{2-x} and MoS₂ with and without CNT backbones. As summarized in Table 4, the j_0 of 1.62 $\mu\text{A cm}^{-2}$ for CNT-MoSe_{1.06}S_{0.94} outperforms the value of 0.39, 0.03, 0.43, 0.72, and 0.95 $\mu\text{A cm}^{-2}$ for MoSe₂, MoS₂, MoSe_{1.05}S_{0.95}, CNT-MoSe₂, and CNT-MoS₂ respectively. The

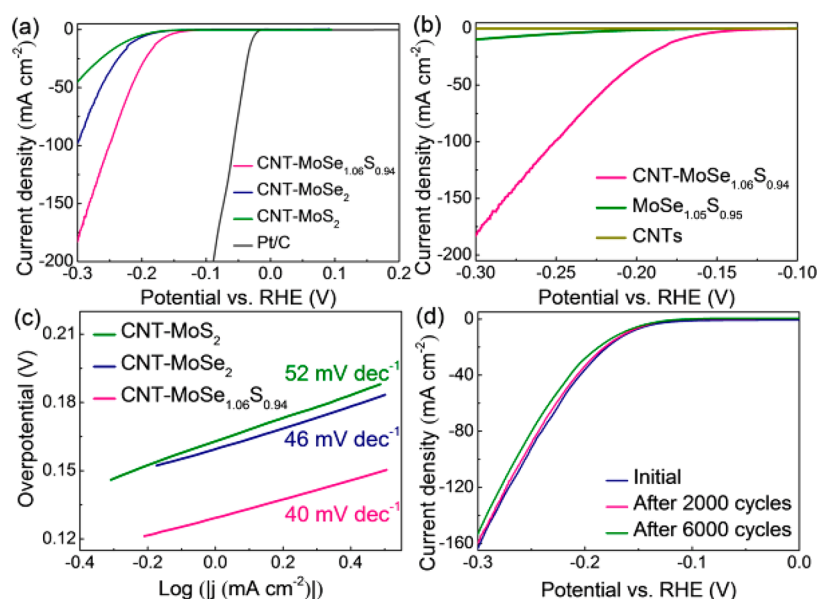


Figure 6. (a) LSV polarization curves of the CNT-MoSe_{1.06}S_{0.94}, CNT-MoSe₂, CNT-MoS₂, and Pt/C at 2 mV s⁻¹. (b) LSV polarization curves of the CNT-MoSe_{1.06}S_{0.94}, MoSe_{1.05}S_{0.95}, and CNTs at 2 mV s⁻¹. (c) Corresponding Tafel plots of the CNT-MoSe_{1.06}S_{0.94}, CNT-MoSe₂, CNT-MoS₂ derived from the polarization curves. (d) Cycling stability of the CNT-MoSe_{1.06}S_{0.94} at 2 mV s⁻¹.

Table 3. Comparison of Catalytic Properties of CNT-MoSe_{1.06}S_{0.94} with MoSe_xS_{2-x}-Based Electrocatalysts in the Literature

catalysts	synthesis method	onset (mV)	$\eta@10 \text{ mA cm}^{-2}$	Tafel slope (mV dec ⁻¹)	refs
CNT@MoSe ₂ nanosheets	solvothermal	-120	202	58	57
MoS ₂ nanosheets/CNTs	hydrothermal reaction	-90	189	44.6	58
MoS _x /NCNT forest	low-temperature decomposition	-75	110	40	55
MoSe ₂ layer/rGO nanosheets	solvothermal	-125	195	67	59
MoS ₂ nanoparticles /rGO sheets	solvothermal	-100	160	41	28
MoSe nanosheets @rGO sheets	self-assembly	-98	155	51	47
Monolayered MoS _{2(1-x)} Se _{2x}	CVD	-182	273	119	12
MoS _{2(1-x)} Se _{2x} Alloy nanoflakes	high-temperature solution reaction	-38	166	48	2
MoS _{2(1-x)} Se _{2x} nanoflakes (HD)/CNFs	CVD	-54	150	144	60
MoS _{2(1-x)} Se _{2x} nanoflakes (LD)/CNFs	CVD	-104	272	124	60
3D MoS _{2(1-x)} Se _{2x} nanosheets	CVD	-98	183	55.5	29
CNT-MoSe _{1.06} S _{0.94}	"all-in-crucible" solid-state sulfidation	-83	174	40	this work

Table 4. Calculated Exchange Current Densities of the MoSe₂, MoSe_{1.05}S_{0.95}, MoS₂, CNT-MoSe₂, CNT-MoSe_{1.06}S_{0.94}, and CNT-MoS₂

catalysts	log($ j \text{ (mA cm}^{-2}\text{)} $) at $\eta = 0 \text{ V}$	exchange current densities j_0 ($\mu\text{A cm}^{-2}$)
MoSe ₂	-3.34	0.39
MoSe _{1.05} S _{0.95}	-3.37	0.43
MoS ₂	-4.48	0.03
CNT-MoSe ₂	-3.14	0.72
CNT-MoSe _{1.06} S _{0.94}	-2.79	1.62
CNT-MoS ₂	-3.02	0.95

lower overpotential and larger exchange current density of CNT-MoSe_{1.06}S_{0.94} reveals an improved inherent HER activity due to the crystal distortion induced by S atomic replacements within MoSe₂, which greatly reduce the free energy of H adsorption and afford more defective active sites. The electrochemical double-layer capacitances (C_{dl}), as an important parameter describing the electrochemical active surface area of a catalyst, are determined by performing the cyclic voltammetry (CV) at the scan rates of 5, 10, 20, 50, 100,

200 mV s⁻¹ in the potential range of 0.1–0.2 V vs RHE. The current density variations ΔJ ($\Delta J = J_{\text{anodic}} - J_{\text{cathodic}}$) at 150 mV vs RHE are plotted against scan rates, and the half slope of fitted line enables the estimation of C_{dl} as shown in Figure S9. The C_{dl} of CNT-MoSe₂, CNT-MoS₂, and CNT-MoSe_{1.06}S_{0.94} are 28.1, 19.8, and 37.6 mF cm⁻², respectively, indicating that the CNT-MoSe_{1.06}S_{0.94} electrode possesses higher effective active surface area than CNT-MoS₂ and CNT-MoSe₂ electrodes. The enhanced electrochemical active surface area manifests the proliferation of exposed active sites. Besides extra defect-rich sites, the enhanced conductivity of the catalyst is also beneficial to enhance the final HER performance. EIS measurements were conducted in the frequency ranging from 1×10^6 Hz to 0.01 Hz at 250 mV vs RHE to study the charge-transfer mechanism during the HER process. The semicircles of the Nyquist plots in Figure S10 indicate that charge-transfer resistance controls the kinetics at the electrode interface. The CNT-MoSe_{1.06}S_{0.94} exhibits the lowest R_{ct} of 47 Ω than that of MoSe₂ (664 Ω), MoSe_xS_{2-x} (564 Ω) and CNT-MoSe₂ (89 Ω), indicating a fast charge transport during the HER process. The remarkable decrease of the charge-transfer resistance may arise from the introduction of highly conductive CNT backbones

and the atomic doping of S atoms into MoSe₂ that enhance the intrinsic conductivity of MoSe₂.

The durability, another significant property to comprehensively assess catalysts for HER, was investigated by conducting the LSV measurements after repeated CV between -0.4 and 0.2 V vs RHE. The polarization curves of the CNT-MoSe_{1.06}S_{0.94} electrode at 2 mV s⁻¹ after 2000 and 6000 cycles were recorded (Figure 6d). Notably, there is no appreciable decay of cathodic current after 2000 cycles, manifesting an outstanding stability of the CNT-MoSe_{1.06}S_{0.94} electrode in acid. After 6000 cycles, the overpotentials lightly increase from 160 to 166 mV at 10 mA cm⁻². The chronoamperometric curve of the CNT-MoSe_{1.06}S_{0.94} electrode at an overpotential of 200 mV in 0.5 M H₂SO₄ was further measured (Figure S11). The negligible deterioration might arise from the consumption of H⁺ in the electrolyte or the production of H₂ bubbles, which are distributed around the electrode and hinder the reactions to continue. The durability of supported catalyst strongly depends on the interactions between the catalytic species and supporting substrates,⁵⁵ indicating that the as-obtained MoSe_{1.06}S_{0.94} nanosheets and the CNT backbones can synergistically give rise to the resultant structural stability during cycling. Figure S12a, b show SEM images of the CNT-MoSe_{1.06}S_{0.94} hybrid after the durability tests. The MoSe_{1.06}S_{0.94} nanosheets did not peel off from the CNT backbones except with little deformations. TEM images (Figure S12c, d) further confirm the structural stability of the decorated MoSe_{1.06}S_{0.94}, indicating an excellent stability of the CNT-MoSe_{1.06}S_{0.94} hybrid catalyst during long-time HER processes. The XRD results were used to test for the changes in crystal structures and compositions of the CNT-MoSe_{1.06}S_{0.94} hybrid before and after 6000 cycles (Figure 13a). The XRD diffraction patterns show quite consistent characteristic peaks with no significant changes after the HER cycling. The XPS spectra of the CNT-MoSe_{1.06}S_{0.94} hybrid after the HER cycling also show no obvious changes of the oxidation states for the Mo, Se, and S (Figure S13b–d). All of these characterizations suggest the excellent stability of the CNT-MoSe_{1.06}S_{0.94} for promising HER applications.

The comparison of the catalytic properties between the CNT-MoSe_xS_{2-x} hybrid and other TMD-based catalysts has been summarized and listed in Table 3. In contrast to other reported TMD-based HER electrocatalysts, the resultant CNT-MoSe_{1.06}S_{0.94} shows a competitive onset overpotential and low overpotential at 10 mA cm⁻². More importantly, our CNT-MoSe_{1.06}S_{0.94} catalysts show the optimal Tafel slope as low as 40 mV dec⁻¹. Considering the environmentally friendly concept for the construction of simple and controllable synthesis route, our study therefore demonstrates great potentials for fabricating potential TMD-based catalysts for efficient electrocatalysis toward HER.

Therefore, the significantly enhanced electrochemical HER activity of the CNT-MoSe_{1.06}S_{0.94} electrode can be ascribed to the following reasons. (1) 1D CNTs not only provide a confined substrate for the decoration of 2D MoSe_{1.06}S_{0.94} with more exposed catalytic sites, but also form interconnected conductive networks and well-defined interior voids for efficiently transferring electrons from glassy carbon electrodes to catalytic active sites of the MoSe_{1.06}S_{0.94} and boosting an efficient diffusion of hydrogen ions onto the MoSe_{1.06}S_{0.94} surface. (2) 2D MoSe_{1.06}S_{0.94} with more crystal distortion and significant residual strain can give rise to the proliferation of defective sites and exposed active sites, which is beneficial for

the improvement of resultant catalytic performance.⁵⁶ (3) The excellent HER catalytic activity of the CNT-MoSe_{1.06}S_{0.94} may result from the modification of the electronic structure of MoSe_xS_{2-x} with an appropriate Se/S ratio, which can achieve the ΔG_{H^*} close to thermoneutral ($\Delta G_{H^*} \approx 0$) and exert a positive effect on the HER activity of resultant catalysts.² The doping of S atoms within MoSe_xS_{2-x} with tunable compositions may also lead to extra donor levels in the forbidden energy gap, which would promote the electronic conductivity due to the narrowed band gap compared with neat MoS₂ and MoSe₂.

4. CONCLUSIONS

In summary, a unique all-in-crucible solid-state sulfidation has been developed for the preparation of the CNT-MoSe_xS_{2-x} hybrid with a tunable Se/S ratio. Compared with conventional solution-processed sulfidation with an extremely low yield and high energy consumption/cost, the solid-state sulfidation provides an easily scalable synthesis of the MoSe_xS_{2-x} nanostructures. The resultant CNT-MoSe_{1.06}S_{0.94} catalysts exhibit largely boosted HER performance including low onset overpotential at 83 mV, low Tafel slope of 40 mV dec⁻¹, and negligible current decay after 6000 cycles. This work therefore opens up new strategies for the design and controllable synthesis of the TMDs and hybrid materials for energy conversation.

■ ASSOCIATED CONTENT

Supporting Information

The Supporting Information is available free of charge on the ACS Publications website at DOI: 10.1021/acsam.8b01466.

Experimental Section, Figures S1–S13, and Table S1 (PDF)

■ AUTHOR INFORMATION

Corresponding Authors

* E-mail: czhang@dhu.edu.cn.

* E-mail: txliu@dhu.edu.cn or txliu@fudan.edu.cn.

* E-mail: ziweixu2014@ujs.edu.cn.

ORCID

Jixin Zhu: 0000-0001-8749-8937

Chao Zhang: 0000-0003-1255-7183

Tianxi Liu: 0000-0002-5592-7386

Notes

The authors declare no competing financial interest.

■ ACKNOWLEDGMENTS

We are grateful for the financial support from the National Natural Science Foundation of China (51433001, 21504012, 51773035, 11774136, and 11404144), the Program of Shanghai Subject Chief Scientist (17XD1400100), the Natural Science Foundation of Shanghai (17ZR1439900), the Shanghai Rising-Star Program (18QA1400200), the China Postdoctoral Science Foundation funded project (2016M601722), and the Shanghai Scientific and Technological Innovation Project (18JC1410600).

■ REFERENCES

(1) Dunn, S. Hydrogen Futures: Toward a Sustainable Energy System. *Int. J. Hydrogen Energy* **2002**, *27*, 235–264.

- (2) Gong, Q. F.; Cheng, L.; Liu, C. H.; Zhang, M.; Feng, Q. L.; Ye, H. L.; Zeng, M.; Xie, L. M.; Liu, Z.; Li, Y. G. Ultrathin MoS₂(1-X)Se₂X Alloy Nanoflakes for Electrocatalytic Hydrogen Evolution Reaction. *ACS Catal.* **2015**, *5*, 2213–2219.
- (3) Liu, Y.; Xiao, C.; Huang, P.; Cheng, M.; Xie, Y. Regulating the Charge and Spin Ordering of Two-Dimensional Ultrathin Solids for Electrocatalytic Water Splitting. *Chem.* **2018**, *4*, 1263–1283.
- (4) Nørskov, J. K.; Bligaard, T.; Logadottir, A.; Kitchin, J.; Chen, J.; Pandelov, S.; Stimming, U. Trends in the Exchange Current for Hydrogen Evolution. *J. Electrochem. Soc.* **2005**, *152*, 23–26.
- (5) Stephens, I. E.; Chorkendorff, I. Minimizing the Use of Platinum in Hydrogen-Evolving Electrodes. *Angew. Chem., Int. Ed.* **2011**, *50*, 1476–1477.
- (6) Jiang, P.; Liu, Q.; Liang, Y.; Tian, J.; Asiri, A. M.; Sun, X. A Cost-Effective 3D Hydrogen Evolution Cathode with High Catalytic Activity: FeP Nanowire Array as the Active Phase. *Angew. Chem., Int. Ed.* **2014**, *53*, 12855–12859.
- (7) Morales-Guio, C. G.; Stern, L.-A.; Hu, X. Nanostructured Hydrotreating Catalysts for Electrochemical Hydrogen Evolution. *Chem. Soc. Rev.* **2014**, *43*, 6555–6569.
- (8) Cao, X.; Tan, C.; Sindoro, M.; Zhang, H. Hybrid Micro-/Nano-Structures Derived from Metal-Organic Frameworks: Preparation and Applications in Energy Storage and Conversion. *Chem. Soc. Rev.* **2017**, *46*, 2660–2677.
- (9) Xu, X.; Shi, W.; Li, P.; Ye, S.; Ye, C.; Ye, H.; Lu, T.; Zheng, A.; Zhu, J.; Xu, L.; Zhong, M.; Cao, X. Facile Fabrication of Three-Dimensional Graphene and Metal–Organic Framework Composites and Their Derivatives for Flexible All-Solid-State Supercapacitors. *Chem. Mater.* **2017**, *29*, 6058–6065.
- (10) Faber, M. S.; Jin, S. Earth-Abundant Inorganic Electrocatalysts and Their Nanostructures for Energy Conversion Applications. *Energy Environ. Sci.* **2014**, *7*, 3519–3542.
- (11) Xu, J.; Zhang, J.; Zhang, W.; Lee, C.-S. Interlayer Nanoarchitectonics of Two-Dimensional Transition-Metal Dichalcogenides Nanosheets for Energy Storage and Conversion Applications. *Adv. Energy Mater.* **2017**, *7*, 1700571.
- (12) Yang, L.; Fu, Q.; Wang, W.; Huang, J.; Huang, J.; Zhang, J.; Xiang, B. Large-Area Synthesis of Monolayered MoS₂ (1-X) Se₂X with a Tunable Band Gap and Its Enhanced Electrochemical Catalytic Activity. *Nanoscale* **2015**, *7*, 10490–10497.
- (13) Zhu, C. R.; Gao, D.; Ding, J.; Chao, D.; Wang, J. TMD-Based Highly Efficient Electrocatalysts Developed by Combined Computational and Experimental Approaches. *Chem. Soc. Rev.* **2018**, *47*, 4332–4356.
- (14) Cao, X.; Tan, C.; Zhang, X.; Zhao, W.; Zhang, H. Solution-Processed Two-Dimensional Metal Dichalcogenide-Based Nanomaterials for Energy Storage and Conversion. *Adv. Mater.* **2016**, *28*, 6167–6196.
- (15) Xie, J.; Zhang, J.; Li, S.; Grote, F.; Zhang, X.; Zhang, H.; Wang, R.; Lei, Y.; Pan, B.; Xie, Y. Controllable Disorder Engineering in Oxygen-Incorporated MoS₂ Ultrathin Nanosheets for Efficient Hydrogen Evolution. *J. Am. Chem. Soc.* **2013**, *135*, 17881–17888.
- (16) Peng, S. J.; Li, L. L.; Han, X. P.; Sun, W. P.; Srinivasan, M.; Mhaisalkar, S. G.; Cheng, F. Y.; Yan, Q. Y.; Chen, J.; Ramakrishna, S. Cobalt Sulfide Nanosheet/Graphene/Carbon Nanotube Nanocomposites as Flexible Electrodes for Hydrogen Evolution. *Angew. Chem., Int. Ed.* **2014**, *53*, 12594–12599.
- (17) Gao, M. R.; Liang, J. X.; Zheng, Y. R.; Xu, Y. F.; Jiang, J.; Gao, Q.; Li, J.; Yu, S. H. An Efficient Molybdenum Disulfide/Cobalt Diselenide Hybrid Catalyst for Electrochemical Hydrogen Generation. *Nat. Commun.* **2015**, *6*, 5982.
- (18) Cheng, L.; Huang, W.; Gong, Q.; Liu, C.; Liu, Z.; Li, Y.; Dai, H. Ultrathin WS₂ Nanoflakes as a High-Performance Electrocatalyst for the Hydrogen Evolution Reaction. *Angew. Chem., Int. Ed.* **2014**, *53*, 7860–7863.
- (19) Xu, C.; Peng, S. J.; Tan, C. L.; Ang, H. X.; Tan, H. T.; Zhang, H.; Yan, Q. Y. Ultrathin S-Doped MoSe₂ Nanosheets for Efficient Hydrogen Evolution. *J. Mater. Chem. A* **2014**, *2*, 5597–5601.
- (20) Jia, L.; Sun, X.; Jiang, Y.; Yu, S.; Wang, C. A Novel MoSe₂–Reduced Graphene Oxide/Polyimide Composite Film for Applications in Electrocatalysis and Photoelectrocatalysis Hydrogen Evolution. *Adv. Funct. Mater.* **2015**, *25*, 1814–1820.
- (21) Kibsgaard, J.; Chen, Z.; Reinecke, B. N.; Jaramillo, T. F. Engineering the Surface Structure of MoS₂ to Preferentially Expose Active Edge Sites for Electrocatalysis. *Nat. Mater.* **2012**, *11*, 963.
- (22) Karunadasa, H. I.; Montalvo, E.; Sun, Y.; Majda, M.; Long, J. R.; Chang, C. J. A Molecular MoS₂ Edge Site Mimic for Catalytic Hydrogen Generation. *Science* **2012**, *335*, 698–702.
- (23) Deng, S.; Zhong, Y.; Zeng, Y.; Wang, Y.; Yao, Z.; Yang, F.; Lin, S.; Wang, X.; Lu, X.; Xia, X.; Tu, J. Directional Construction of Vertical Nitrogen-Doped 1T-2H MoSe₂/Graphene Shell/Core Nanoflake Arrays for Efficient Hydrogen Evolution Reaction. *Adv. Mater.* **2017**, *29*, 1700748.
- (24) Najafi, L.; Bellani, S.; Oropesa-Nuñez, R.; Ansaldo, A.; Prato, M.; Del Rio Castillo, A. E.; Bonaccorso, F. Engineered MoSe₂-Based Heterostructures for Efficient Electrochemical Hydrogen Evolution Reaction. *Adv. Energy Mater.* **2018**, *8*, 1703212.
- (25) Masurkar, N.; Thangavel, N. K.; Arava, L. M. R. CVD-Grown MoSe₂ Nanoflowers with Dual Active Sites for Efficient Electrochemical Hydrogen Evolution Reaction. *ACS Appl. Mater. Interfaces* **2018**, *10*, 27771–27779.
- (26) Damien, D.; Anil, A.; Chatterjee, D.; Shaijumon, M. Direct Deposition of MoSe₂ Nanocrystals onto Conducting Substrates: Towards Ultra-Efficient Electrocatalysts for Hydrogen Evolution. *J. Mater. Chem. A* **2017**, *5*, 13364–13372.
- (27) Park, G. D.; Kim, J. H.; Park, S.-K.; Kang, Y. C. MoSe₂ Embedded CNT-Reduced Graphene Oxide Composite Microsphere with Superior Sodium Ion Storage and Electrocatalytic Hydrogen Evolution Performances. *ACS Appl. Mater. Interfaces* **2017**, *9*, 10673–10683.
- (28) Li, Y.; Wang, H.; Xie, L.; Liang, Y.; Hong, G.; Dai, H. MoS₂ Nanoparticles Grown on Graphene: An Advanced Catalyst for the Hydrogen Evolution Reaction. *J. Am. Chem. Soc.* **2011**, *133*, 7296–7299.
- (29) Chen, X.; Wang, Z.; Qiu, Y.; Zhang, J.; Liu, G.; Zheng, W.; Feng, W.; Cao, W.; Hu, P.; Hu, W. Controlled Growth of Vertical 3D MoS₂ (1-X) Se₂X Nanosheets for an Efficient and Stable Hydrogen Evolution Reaction. *J. Mater. Chem. A* **2016**, *4*, 18060–18066.
- (30) Chen, X.; Liu, G.; Zheng, W.; Feng, W.; Cao, W.; Hu, W.; Hu, P. A Vertical 2D MoO₂/MoSe₂ Core–Shell Nanosheet Arrays as High-Performance Electrocatalysts for Hydrogen Evolution Reaction. *Adv. Funct. Mater.* **2016**, *26*, 8537–8544.
- (31) Zhang, J.; Wu, M. H.; Shi, Z. T.; Jiang, M.; Jian, W. J.; Xiao, Z.; Li, J.; Lee, C. S.; Xu, J. Composition and Interface Engineering of Alloyed MoS₂ X Se₂(1-X) Nanotubes for Enhanced Hydrogen Evolution Reaction Activity. *Small* **2016**, *12*, 4379–4385.
- (32) Liu, K.; Zhang, W.; Lei, F.; Liang, L.; Gu, B.; Sun, Y.; Ye, B.; Ni, W.; Xie, Y. Nitrogen-Doping Induced Oxygen Vacancies in Freestanding Molybdenum Trioxide Single-Layers Boosting Electrocatalytic Hydrogen Evolution. *Nano Energy* **2016**, *30*, 810–817.
- (33) Gurker, N.; Ebel, M. F.; Ebel, H. Imaging XPS—a New Technique, I—Principles. *Surf. Interface Anal.* **1983**, *5*, 13–19.
- (34) Vohrer, U.; Blomfield, C.; Page, S.; Roberts, A. Quantitative XPS Imaging—New Possibilities with the Delay-Line Detector. *Appl. Surf. Sci.* **2005**, *252*, 61–65.
- (35) Ammann, A. A. Inductively Coupled Plasma Mass Spectrometry (ICP-MS): A Versatile Tool. *J. Mass Spectrom.* **2007**, *42*, 419–427.
- (36) Olesik, J. W. Elemental Analysis Using ICP-OES and ICP/MS. *Anal. Chem.* **1991**, *63*, 12A–21A.
- (37) Greeley, J.; Jaramillo, T. F.; Bonde, J.; Chorkendorff, I. B.; Nørskov, J. K. Computational High-Throughput Screening of Electrocatalytic Materials for Hydrogen Evolution. *Nat. Mater.* **2006**, *5*, 909–913.
- (38) Zheng, Y.; Jiao, Y.; Jaroniec, M.; Qiao, S. Z. Advancing the Electrochemistry of the Hydrogen-Evolution Reaction through

Combining Experiment and Theory. *Angew. Chem., Int. Ed.* **2015**, *54*, 52–65.

(39) Jaramillo, T. F.; Jorgensen, K. P.; Bonde, J.; Nielsen, J. H.; Horch, S.; Chorkendorff, I. Identification of Active Edge Sites for Electrochemical H₂ Evolution from MoS₂ Nanocatalysts. *Science* **2007**, *317*, 100–102.

(40) Karunadasa, H. I.; Montalvo, E.; Sun, Y.; Majda, M.; Long, J. R.; Chang, C. J. A Molecular MoS(2) Edge Site Mimic for Catalytic Hydrogen Generation. *Science* **2012**, *335*, 698–702.

(41) Voiry, D.; Salehi, M.; Silva, R.; Fujita, T.; Chen, M.; Asefa, T.; Shenoy, V. B.; Eda, G.; Chhowalla, M. Conducting MoS(2) Nanosheets as Catalysts for Hydrogen Evolution Reaction. *Nano Lett.* **2013**, *13*, 6222–6227.

(42) Hinnemann, B.; Moses, P. G.; Bonde, J.; Jorgensen, K. P.; Nielsen, J. H.; Horch, S.; Chorkendorff, I.; Nørskov, J. K. Biomimetic Hydrogen Evolution: MoS₂ Nanoparticles as Catalyst for Hydrogen Evolution. *J. Am. Chem. Soc.* **2005**, *127*, 5308–5309.

(43) Tang, H.; Dou, K.; Kaun, C.-C.; Kuang, Q.; Yang, S. MoSe₂ nanosheets and Their Graphene Hybrids: Synthesis, Characterization and Hydrogen Evolution Reaction Studies. *J. Mater. Chem. A* **2014**, *2*, 360–364.

(44) Chen, Y.; Wang, J.; Liu, H.; Li, R.; Sun, X.; Ye, S.; Knights, S. Enhanced Stability of Pt Electrocatalysts by Nitrogen Doping in CNTs for PEM Fuel Cells. *Electrochem. Commun.* **2009**, *11*, 2071–2076.

(45) Ouyang, Y.; Ling, C.; Chen, Q.; Wang, Z.; Shi, L.; Wang, J. Activating Inert Basal Planes of MoS₂ for Hydrogen Evolution Reaction through the Formation of Different Intrinsic Defects. *Chem. Mater.* **2016**, *28*, 4390–4396.

(46) Tsai, C.; Abild-Pedersen, F.; Nørskov, J. K. Tuning the MoS(2) Edge-Site Activity for Hydrogen Evolution Via Support Interactions. *Nano Lett.* **2014**, *14*, 1381–1387.

(47) Konkana, B.; Masa, J.; Xia, W.; Muhler, M.; Schuhmann, W. MoSSe@ Reduced Graphene Oxide Nanocomposite Heterostructures as Efficient and Stable Electrocatalysts for the Hydrogen Evolution Reaction. *Nano Energy* **2016**, *29*, 46–53.

(48) Kiran, V.; Mukherjee, D.; Jenjeti, R. N.; Sampath, S. Active Guests in the MoS₂/MoSe₂ Host Lattice: Efficient Hydrogen Evolution Using Few-Layer Alloys of MoS₂(1-X)Se_{2x}. *Nanoscale* **2014**, *6*, 12856–12863.

(49) Mann, J.; Ma, Q.; Odenthal, P. M.; Isarraraz, M.; Le, D.; Preciado, E.; Barroso, D.; Yamaguchi, K.; von Son Palacio, G.; Nguyen, A.; et al. 2-Dimensional Transition Metal Dichalcogenides with Tunable Direct Band Gaps: MoS₂(1-X)Se_{2x} Monolayers. *Adv. Mater.* **2014**, *26*, 1399–1404.

(50) Yang, Y.; Wang, S.; Zhang, J.; Li, H.; Tang, Z.; Wang, X. Nanosheet-Assembled MoSe₂ and S-Doped MoSe₂-X Nanostructures for Superior Lithium Storage Properties and Hydrogen Evolution Reactions. *Inorg. Chem. Front.* **2015**, *2*, 931–937.

(51) Feng, Q.; Zhu, Y.; Hong, J.; Zhang, M.; Duan, W.; Mao, N.; Wu, J.; Xu, H.; Dong, F.; Lin, F.; et al. Growth of Large-Area 2D MoS₂ (1-X) Se_{2x} Semiconductor Alloys. *Adv. Mater.* **2014**, *26*, 2648–2653.

(52) Kamada, R.; Yagioka, T.; Adachi, S.; Handa, A.; Tai, K. F.; Kato, T.; Sugimoto, H. New World Record Cu (in, Ga)(Se, S) 2 Thin Film Solar Cell Efficiency Beyond 22%. In *43rd IEEE Photovoltaic Specialists Conference (PVSC)*; IEEE, 2016; pp 1287–1291.

(53) Mansfeld, F. Tafel Slopes and Corrosion Rates Obtained in the Pre-Tafel Region of Polarization Curves. *Corros. Sci.* **2005**, *47*, 3178–3186.

(54) Merki, D.; Hu, X. Recent Developments of Molybdenum and Tungsten Sulfides as Hydrogen Evolution Catalysts. *Energy Environ. Sci.* **2011**, *4*, 3878–3888.

(55) Li, D. J.; Maiti, U. N.; Lim, J.; Choi, D. S.; Lee, W. J.; Oh, Y.; Lee, G. Y.; Kim, S. O. Molybdenum Sulfide/N-Doped Cnt Forest Hybrid Catalysts for High-Performance Hydrogen Evolution Reaction. *Nano Lett.* **2014**, *14*, 1228–1233.

(56) Yang, W.; Zhang, L.; Xie, J.; Zhang, X.; Liu, Q.; Yao, T.; Wei, S.; Zhang, Q.; Xie, Y. Enhanced Photoexcited Carrier Separation in

Oxygen-Doped ZnIn₂S₄ Nanosheets for Hydrogen Evolution. *Angew. Chem., Int. Ed.* **2016**, *55*, 6716–6720.

(57) Huang, Y.; Lu, H.; Gu, H.; Fu, J.; Mo, S.; Wei, C.; Miao, Y. E.; Liu, T. X. A CNT@MoSe₂ Hybrid Catalyst for Efficient and Stable Hydrogen Evolution. *Nanoscale* **2015**, *7*, 18595–18602.

(58) Yuan, H.; Li, J.; Yuan, C.; He, Z. Facile Synthesis of MoS₂@CNT as an Effective Catalyst for Hydrogen Production in Microbial Electrolysis Cells. *ChemElectroChem* **2014**, *1*, 1828–1833.

(59) Liu, Z.; Li, N.; Zhao, H.; Du, Y. Colloidally Synthesized MoSe₂/Graphene Hybrid Nanostructures as Efficient Electrocatalysts for Hydrogen Evolution. *J. Mater. Chem. A* **2015**, *3*, 19706–19710.

(60) Yang, H.; Zhang, T.; Zhu, H.; Zhang, M.; Wu, W.; Du, M. Synthesis of a MoS₂(1-X)Se_{2x} Ternary Alloy on Carbon Nanofibers as the High Efficient Water Splitting Electrocatalyst. *Int. J. Hydrogen Energy* **2017**, *42*, 1912–1918.